



Deeply virtual Compton scattering using a positron beam in Hall-C at Jefferson Lab

A. Afanasev⁹, I. Albayrak²², S. Ali⁴, M. Amaryan⁶, J. R. M. Annand¹², A. Asaturyan⁵, V. Bellini¹⁶, V. V. Berdnikov⁴, M. Boer¹⁰, K. Brinkmann¹⁴, W. J. Briscoe⁹, A. Camsonne¹, M. Caudron², L. Causse², M. Carmignotto¹, D. Day¹³, M. Defurne²⁴, S. Diehl¹⁴, R. Ent¹, P. Chatagnon², R. Dupré², D. Dutta¹⁷, M. Ehrhart², M. A. I. Fernando²³, T. Forest¹¹, M. Guidal², J. Grames¹, P. Gueye¹⁵, S. Habet², D. J. Hamilton¹², A. Hobart², T. Horn⁴, C. Hyde⁶, G. Kalicy⁴, D. Keller¹³, C. Keppel¹, M. Kerver⁶, E. Kinney¹⁸, H.-S. Ko², D. Marchand², P. Markowitz⁸, M. Mazouz³, M. McCaughan¹, B. McKinnon¹², A. Mkrtchyan⁵, H. Mkrtchyan⁵, M. Muhoza⁴, C. Muñoz Camacho^{2,a}, J. Murphy⁷, P. Nadel-Turonski¹⁹, S. Niccolai², G. Niculescu²⁰, R. Novotny¹⁴, R. Paremuzyan¹⁰, I. Pegg⁴, K. Price², H. Rashad⁶, J. Roche⁷, R. Rondon¹³, B. Sawatzky¹, V. Sergeyeva², S. Širca²¹, A. Somov¹, I. Strakovsky⁹, V. Tadevosyan⁵, R. Trotta⁴, H. Voskanyan⁵, E. Voutier², B. Wojtsekhowski¹, S. Wood¹, S. Zhamkochyan⁵, J. Zhang¹³, S. Zhao², C. Zorn¹

¹ Thomas Jefferson National Accelerator Facility, 12000 Jefferson Avenue, Newport News, VA 23606, USA

² Université Paris-Saclay, CNRS/IN2P3, IJCLab, Orsay, France

³ Faculté des Sciences de Monastir, Bitola, Tunisia

⁴ The Catholic University of America, Washington, DC 20064, USA

⁵ A. Alikhanyan National Laboratory, Yerevan Physics Institute, Yerevan 375036, Armenia

⁶ Old Dominion University, Norfolk, VA 23529, USA

⁷ Ohio University, Athens, OH 45701, USA

⁸ Florida International University, Miami, FL 33199, USA

⁹ The George Washington University, Washington, DC 20052, USA

¹⁰ University of New Hampshire, Durham, NH 03824, USA

¹¹ Idaho State University, Pocatello, ID 83209, USA

¹² University of Glasgow, Glasgow G12 8QQ, UK

¹³ University of Virginia, Charlottesville, VA 22904, USA

¹⁴ Universität Gießen Ludwigstraße 23, 35390 Giessen, Deutschland

¹⁵ Facility for Rare Isotope Beams, Michigan State University, 640 South Shaw Lane, East Lansing, MI 48824, USA

¹⁶ Istituto Nazionale di Fisica Nucleare, Sezione di Catania, 95123 Catania, Italy

¹⁷ Mississippi State University, Starkville, MS 39762, USA

¹⁸ University of Colorado, Boulder, CO 80309, USA

¹⁹ Stony Brook University, Stony Brook, NY 11794, USA

²⁰ James Madison University, Harrisonburg, VA 22807, USA

²¹ Faculty of Mathematics and Physics, University of Ljubljana, 1000 Ljubljana, Slovenia

²² Akdeniz Üniversitesi, Konyaaltı, 07070 Antalya, Turkey

²³ Hampton University Hampton, Hampton, VA 23668, USA

²⁴ Commissariat à l'Energie Atomique, 91191 Gif-sur-Yvette, France

Received: 13 May 2021 / Accepted: 26 August 2021 / Published online: 29 October 2021

© The Author(s), under exclusive licence to Società Italiana di Fisica and Springer-Verlag GmbH Germany, part of Springer Nature 2021
Communicated by Nicolas Alamanos

Abstract We propose to use the High Momentum Spectrometer of Hall C combined with the Neutral Particle Spectrometer (NPS) to perform high precision measurements of the Deeply Virtual Compton Scattering (DVCS) cross section using a beam of positrons. The combination of measurements with oppositely charged incident beams is the only unambiguous way to disentangle the contribution of the DVCS²

term in the photon electroproduction cross section from its interference with the Bethe-Heitler amplitude. This provides a stronger way to constrain the Generalized Parton Distributions of the nucleon. A wide range of kinematics accessible with an 11 GeV beam off an unpolarized proton target will be covered. The Q^2 -dependence of each contribution will be measured independently.

^a e-mail: munoz@ijclab.in2p3.fr (corresponding author)

1 Executive summary

An exciting scientific frontier is the 3-dimensional exploration of nucleon (and nuclear) structure – nuclear femtography. Jefferson Lab with its high luminosity and expanded kinematic reach at 12-GeV will allow the detailed investigation of position and momentum distributions of partons inside protons and neutrons in the valence-quark region. The study of the Generalized Parton Distributions (GPDs) captures the images of the transverse position distributions of fast-moving quarks. The cleanest reaction to access GPDs is Deeply Virtual Compton Scattering (DVCS): $\gamma^* p \rightarrow \gamma p$.

A factorization theorem has been proven for DVCS in the Bjorken limit [1,2]. It allows one to compute the DVCS amplitude as the product of some GPDs and a coefficient function that can be calculated perturbatively. GPDs are thus in very solid theoretical footing: at leading-twist level, all-order QCD-factorization theorems directly relate the GPDs to particular hard exclusive scattering processes. Therefore, GPDs are process-independent, universal quantities.

DVCS interferes with the so-called Bethe–Heitler (BH) process, where the lepton scatters elastically off the nucleon and emits a high energy photon before or after the interaction (see Fig. 1). The BH amplitude \mathcal{T}^{BH} is electron charge even. On the other hand, the DVCS amplitude \mathcal{T}^{DVCS} is electric charge odd, i.e. its contribution has different sign for electron vs. positron scattering. DVCS and BH are indistinguishable and the photon electroproduction amplitude squared that we can measure is therefore decomposed as:

$$|\mathcal{T}(\pm ep \rightarrow \pm e p \gamma)|^2 = |\mathcal{T}^{BH}|^2 + |\mathcal{T}^{DVCS}|^2 \mp \mathcal{I}, \quad (1)$$

where the \pm signs correspond to the charge of the incident beam. The \mathcal{T}^{BH} amplitude is written in terms of the nucleon form factors, and is real at the leading order in QED. The $|\mathcal{T}^{DVCS}|^2$ contribution is closest to a direct Compton scattering cross section and as such gives direct information on nucleon structure - it depends on bilinear combinations of GPDs.

Equation 1 shows how combining DVCS measurements with electrons and positrons not only can cleanly isolate the $|\mathcal{T}^{DVCS}|^2$ term but also the interference term \mathcal{I} . This interference term gives direct linear access to DVCS at the amplitude level, thanks to its interference with the known Bethe–

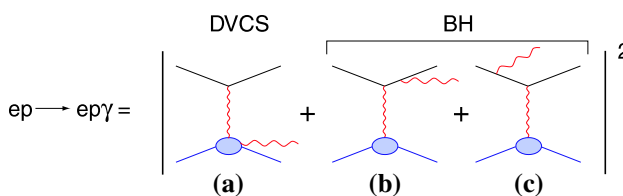


Fig. 1 Illustration of the DVCS (a) and Bethe–Heitler (b and c) processes

Heitler amplitude. Similar as in spin-dependent scattering, such interferences can lead to extremely rich angular structure: $\mathcal{I} = 2\mathcal{T}^{BH}\mathcal{R}](\mathcal{T}^{DVCS})$.

The availability of positron beams thus can lead to direct access to nucleon structure carried in the DVCS amplitude, and in addition a cleaner access to the $|\mathcal{T}^{DVCS}|^2$ term.

2 Introduction

Deeply Virtual Compton Scattering (DVCS) refers to the reaction $\gamma^*(q)P(p) \rightarrow P(p')\gamma(q')$ in the Bjorken limit of Deep Inelastic Scattering (DIS). Experimentally, we can access DVCS through electroproduction of real photons $e(k)P(p) \rightarrow e(k')P(p')\gamma(q')$, where the DVCS amplitude interferes with the so-called Bethe–Heitler (BH) process. The BH contribution is calculable in QED since it corresponds to the emission of the photon by the incoming or the outgoing electron.

DVCS is the simplest probe of a new class of light-cone (quark) matrix elements, called Generalized Parton Distributions (GPDs) [5]. The GPDs offer the exciting possibility of the first ever spatial images of the quark waves inside the proton, as a function of their wavelength [3–8]. The correlation of transverse spatial and longitudinal momentum information contained in the GPDs provides a new tool to evaluate the contribution of quark orbital angular momentum to the proton spin.

GPDs enter the DVCS cross section through integrals over the quark momentum fraction x , called Compton Form Factors (CFFs). CFFs are defined in terms of the vector GPDs H and E , and the axial vector GPDs \tilde{H} and \tilde{E} [5]. For example ($f \in \{u, d, s\}$) [9]:

$$\begin{aligned} \mathcal{H}(\xi, t) = \sum_f \left[\frac{e_f}{e} \right]^2 & \left\{ i\pi [H_f(\xi, \xi, t) - H_f(-\xi, \xi, t)] \right. \\ & \left. + \mathcal{P} \int_{-1}^{+1} dx \left[\frac{1}{\xi - x} - \frac{1}{\xi + x} \right] H_f(x, \xi, t) \right\}, \end{aligned} \quad (2)$$

where $t = (p - p')^2$ is the momentum transfer to the nucleon and skewness variable ξ is defined as $\xi = -\bar{q}^2/(\bar{q} \cdot \bar{p}) \approx x_B/(2 - x_B)$, with $\bar{q} = (q + q')/2$ and $\bar{p} = p + p'$.

Thus, the imaginary part accesses GPDs along the line $x = \pm\xi$, whereas the real part probes GPD integrals over x . The ‘diagonal’ GPD, $H(\xi, \xi, t = \Delta^2)$ is not a positive-definite probability density, however it is a transition density with the momentum transfer Δ_\perp Fourier-conjugate to the transverse distance r between the active parton and the center-of-momentum of the spectator partons in the target [10]. Furthermore, the real part of the Compton Form Factor is determined by a dispersion integral over the diagonal $x = \pm\xi$ plus the D -term [11–14]:

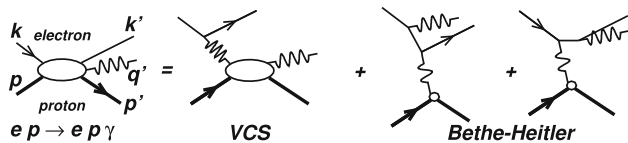


Fig. 2 Lowest order QED amplitude for the $ep \rightarrow e p \gamma$ reaction. The momentum four-vectors of all external particles are labeled at left. The net four-momentum transfer to the proton is $\Delta_\mu = (q - q')_\mu = (p' - p)_\mu$. In the virtual Compton scattering (VCS) amplitude, the (spacelike) virtuality of the incident photon is $Q^2 = -q^2 = -(k - k')^2$. In the Bethe–Heitler (BH) amplitude, the virtuality of the incident photon is $-\Delta^2 = -t$. Standard (e, e') invariants are $s_e = (k + p)^2$, $x_B = Q^2/(2q \cdot p)$ and $W^2 = (q + p)^2$

$$\Re e [\mathcal{H}(\xi, t)]$$

$$= \int_{-1}^1 dx \left\{ [H(x, x, t) + H(-x, x, t)] \right. \\ \left. \times \left[\frac{1}{\xi - x} - \frac{1}{\xi + x} \right] + 2 \frac{D(x, t)}{1 - x} \right\} \quad (3)$$

The D -term [15] only has support in the region $|x| < \xi$ in which the GPD is determined by $q\bar{q}$ exchange in the t -channel.

3 Physics goals

In this experiment we propose to exploit the charge dependence provided by the use of a positron beam in order to cleanly separate the DVCS² term from the DVCS–BH interference in the photon electroproduction cross section.

The photon electroproduction cross section of a polarized lepton beam of energy E_b off an unpolarized target of mass M is sensitive to the coherent interference of the DVCS amplitude with the Bethe–Heitler amplitude (see Fig. 2). It was derived in [4] and can be written as:

$$\frac{d^5\sigma(\lambda, \pm e)}{d^5\Phi} = \frac{d\sigma_0}{dQ^2 dx_B} \left| \mathcal{T}^{BH}(\lambda) \pm \mathcal{T}^{DVCS}(\lambda) \right|^2 / |e|^6 \\ = \frac{d\sigma_0}{dQ^2 dx_B} \left[\left| \mathcal{T}^{BH}(\lambda) \right|^2 + \left| \mathcal{T}^{DVCS}(\lambda) \right|^2 \mp \mathcal{I}(\lambda) \right] \frac{1}{|e|^6} \\ \frac{d\sigma_0}{dQ^2 dx_B} = \frac{\alpha_{\text{QED}}^3}{16\pi^2 (s_e - M^2)^2 x_B} \frac{1}{\sqrt{1 + \epsilon^2}} \\ \epsilon^2 = 4M^2 x_B^2 / Q^2 \\ s_e = 2ME_b + M^2 \quad (4)$$

where $d^5\Phi = dQ^2 dx_B d\phi_e dt d\phi_{\gamma\gamma}$, λ is the electron helicity and the $(+/-)$ stands for the sign of the charge of the lepton beam. The BH contribution is calculable in QED, given our $\approx 1\%$ knowledge of the proton elastic form factors at small momentum transfer. The other two contributions to the cross section, the interference and the DVCS² terms, provide complementary information on GPDs. It is possible to exploit the structure of the cross section as a function of the angle $\phi_{\gamma\gamma}$

between the leptonic and hadronic plane to separate up to a certain degree the different contributions to the total cross section [16]. The angular separation can be supplemented by an beam energy separation. The energy separation has been successfully used in previous experiments [17] at 6 GeV and is the goal of already approved experiment at 12 GeV [18].

The $|\mathcal{T}^{BH}|^2$ term is given in [9], Eq. (25), and only its general form is reproduced here:

$$|\mathcal{T}^{BH}|^2 = \frac{e^6}{x_B^2 t y^2 (1 + \epsilon^2)^2 \mathcal{P}_1(\phi_{\gamma\gamma}) \mathcal{P}_2(\phi_{\gamma\gamma})} \\ \sum_{n=0}^2 c_n^{BH} \cos(n\phi_{\gamma\gamma}). \quad (5)$$

The harmonic terms c_n^{BH} depend upon bilinear combinations of the ordinary elastic form factors $F_1(t)$ and $F_2(t)$ of the proton. The factors \mathcal{P}_i are the electron propagators in the BH amplitude [9].

The interference term in Eq. (4) is a linear combination of GPDs, whereas the DVCS² term is a bilinear combination of GPDs. These terms have the following harmonic structure:

$$\mathcal{I} = \frac{e^6}{x_B y^3 \mathcal{P}_1(\phi_{\gamma\gamma}) \mathcal{P}_2(\phi_{\gamma\gamma}) t} \\ \times \left\{ c_0^{\mathcal{I}} + \sum_{n=1}^3 \left[c_n^{\mathcal{I}} \cos(n\phi_{\gamma\gamma}) + \lambda s_n^{\mathcal{I}} \sin(n\phi_{\gamma\gamma}) \right] \right\} \quad (6)$$

$$\left| \mathcal{T}^{DVCS}(\lambda) \right|^2 = \frac{e^6}{y^2 Q^2} \\ \times \left\{ c_0^{DVCS} + \sum_{n=1}^2 \left[c_n^{DVCS} \cos(n\phi_{\gamma\gamma}) - \lambda s_n^{DVCS} \sin(n\phi_{\gamma\gamma}) \right] \right\} \quad (7)$$

The $c_0^{DVCS,\mathcal{I}}$, and $(c, s)_1^{\mathcal{I}}$ harmonics are dominated by twist-two GPD terms, although they do have twist-three admixtures that must be quantified by the Q^2 -dependence of each harmonic. The $(c, s)_1^{DVCS}$ and $(c, s)_2^{\mathcal{I}}$ harmonics are dominated by twist-three matrix elements, although the same twist-two GPD terms also contribute (but with smaller kinematic coefficients than in the lower Fourier terms). The $(c, s)_2^{DVCS}$ and $(c, s)_3^{\mathcal{I}}$ harmonics stem from twist-two double helicity-flip gluonic GPDs alone. They are formally suppressed by α_s and will be neglected here. They do not mix, however, with the twist-two quark amplitudes. The exact expressions of these harmonics in terms of the quark Compton Form Factors (CFFs) of the nucleon are given in [19].

Equation (4) shows how a positron beam, together with measurements with electrons, provides a way to separate without any assumptions the DVCS² and BH–DVCS interference contributions to the cross section. With electrons alone, the only approach to this separation is to use the different beam energy dependence of the DVCS² and BH–

DVCS interference. This is the strategy that will be used in approved experiment E12-13-010. However, as recent results have shown [17] this technique has limitations due to the need to include power corrections to fully describe the precise azimuthal dependence of the DVCS cross sections.

A positron beam, on the other hand, will be able to pin down each individual term. The Q^2 -dependence of each of them can later be used to study the nature of the higher twist contributions by comparing it to the predictions of the leading twist diagram.

A positron beam can also be used to measure the corresponding beam charge asymmetry defined as:

$$A_C(\phi_{\gamma\gamma}) = \frac{d\sigma^+(\phi_{\gamma\gamma}) - d\sigma^-(\phi_{\gamma\gamma})}{d\sigma^+(\phi_{\gamma\gamma}) + d\sigma^-(\phi_{\gamma\gamma})}, \quad (8)$$

which is easier experimentally. This measurement was pioneered by the HERMES collaboration [20]. A drawback, however, is that it depends non-linearly on the DVCS amplitudes because of the denominator. One can further project the beam charge asymmetry on the various harmonics:

$$A_C^{\cos(n\phi)} = \frac{2 - \delta_{n0}}{2\pi} \int_{-\pi}^{\pi} d\phi_{\gamma\gamma} \cos(n\phi_{\gamma\gamma}) A_C(\phi_{\gamma\gamma}), \quad (9)$$

The $A_C^{\cos(n\phi)}$ is governed by the $c_n^{\mathcal{I}}$ of Eq. (6). Nonetheless, because of the $\phi_{\gamma\gamma}$ -dependent denominator in (8), it is contaminated by all other harmonics as well [21]. Absolute cross-section measurements are thus needed to cleanly measure the interference term without any contamination.

GPDs appear in the DVCS cross section under convolution integrals, usually called Compton Form Factors (CFFs): $\mathcal{F}_{\mu\nu}$, where μ and ν are the helicity states of the virtual photon and the outgoing real photon, respectively. The interference between BH and DVCS provides a way to independently access the real and imaginary parts of CFFs. At leading-order, the imaginary part of the helicity-conserving \mathcal{F}_{++} is directly related to the corresponding GPD at $x = \xi$:

$$\begin{aligned} \mathcal{R}e \mathcal{F}_{++} &= \mathcal{P} \int_{-1}^1 dx \left[\frac{1}{x - \xi} - \kappa \frac{1}{x + \xi} \right] F(x, \xi, t), \\ \mathcal{I}m \mathcal{F}_{++} &= -\pi [F(\xi, \xi, t) + \kappa F(-\xi, \xi, t)], \end{aligned} \quad (10)$$

where $\kappa = -1$ if $F \in \{H, E\}$ and 1 if $F \in \{\tilde{H}, \tilde{E}\}$. Recent phenomenology uses the leading-twist (LT) and leading-order (LO) approximation in order to extract or parametrize GPDs, which translates into neglecting \mathcal{F}_{0+} and \mathcal{F}_{-+} and using the relations of Eq. 10 [22–24].

The scattering amplitude is a Lorentz invariant quantity, but the deeply virtual scattering process nonetheless defines a preferred axis (light-cone axis) for describing the scattering process. At finite Q^2 and non-zero t , there is an ambiguity in defining this axis, though all definitions converge as $Q^2 \rightarrow \infty$ at fixed t . Belitsky et al. [25] decompose the DVCS amplitude in terms of photon-helicity states where the light-

cone axis is defined in the plane of the four-vectors q and P . This leads to the CFFs defined previously. Recently, Braun et al. [21] proposed an alternative decomposition which defines the light cone axis in the plane formed by q and q' and argue that this is more convenient to account for kinematical power corrections of $\mathcal{O}(t/Q^2)$ and $\mathcal{O}(M^2/Q^2)$. The bulk of these corrections can be included by rewriting the CFFs $\mathcal{F}_{\mu\nu}$ in terms of $\mathbb{F}_{\mu\nu}$ using the following map [21]:

$$\mathcal{F}_{++} = \mathbb{F}_{++} + \frac{\chi}{2} [\mathbb{F}_{++} + \mathbb{F}_{-+}] - \chi_0 \mathbb{F}_{0+}, \quad (11)$$

$$\mathcal{F}_{-+} = \mathbb{F}_{-+} + \frac{\chi}{2} [\mathbb{F}_{++} + \mathbb{F}_{-+}] - \chi_0 \mathbb{F}_{0+}, \quad (12)$$

$$\mathcal{F}_{0+} = -(1 + \chi) \mathbb{F}_{0+} + \chi_0 [\mathbb{F}_{++} + \mathbb{F}_{-+}], \quad (13)$$

where kinematic parameters χ_0 and χ are defined as follows (Eq. 48 of Ref. [21]):

$$\chi_0 = \frac{\sqrt{2} Q \tilde{K}}{\sqrt{1 + \epsilon^2}(Q^2 + t)} \propto \frac{\sqrt{t_{min} - t}}{Q}, \quad (14)$$

$$\chi = \frac{Q^2 - t + 2x_B t}{\sqrt{1 + \epsilon^2}(Q^2 + t)} - 1 \propto \frac{t_{min} - t}{Q^2}. \quad (15)$$

Within the $\mathbb{F}_{\mu\nu}$ -parametrization, the leading-twist and leading-order approximation consists in keeping \mathbb{F}_{++} and neglecting both \mathbb{F}_{0+} and \mathbb{F}_{-+} . Nevertheless, as a consequence of Eqs. (12) and (13), \mathcal{F}_{0+} and \mathcal{F}_{-+} are no longer equal to zero since proportional to \mathbb{F}_{++} . The functions that can be extracted from data to describe the three dimensional structure of the nucleon become:

$$\mathcal{F}_{++} = (1 + \frac{\chi}{2}) \mathbb{F}_{++}, \quad \mathcal{F}_{0+} = \chi_0 \mathbb{F}_{++}, \quad \mathcal{F}_{-+} = \frac{\chi}{2} \mathbb{F}_{++}. \quad (16)$$

A numerical application gives $\chi_0 = 0.25$ and $\chi = 0.06$ for $Q^2 = 2 \text{ GeV}^2$, $x_B = 0.36$ and $t = -0.24 \text{ GeV}^2$. Considering the large size of the parameters χ_0 and χ , these kinematical power corrections cannot be neglected in precision DVCS phenomenology, in particular in order to unambiguously extract the CFFs. Indeed, when the beam energy changes, not only do the contributions of the DVCS-BH interference and DVCS² terms change but also the polarization of the virtual photon changes, thereby modifying the weight of the different helicity amplitudes.

The calculation of power corrections to DVCS is one of the most important theory advances in DVCS in recent years. BMP [21] have convincingly shown that in JLab kinematics target mass corrections can be sizeable and cannot be neglected.

4 Experimental setup

We propose to make a precision coincidence setup measuring charged particles (scattered positrons) with the existing HMS and photons using the Neutral Particle Spectrometer (NPS),

currently under construction. The NPS facility consists of a PbWO_4 crystal calorimeter and a sweeping magnet in order to reduce electromagnetic backgrounds. A high luminosity spectrometer and calorimeter (HMS + PbWO_4) combination proposed in Hall C is ideally suited for such measurements.

The sweeping magnet will allow to achieve low-angle photon detection. Detailed background simulations show that this setup allows for $\geq 10\mu\text{A}$ beam current on a 10 cm long cryogenic LH₂ target at the very smallest NPS angles, and much higher luminosities at larger γ, π^0 angles [18].

4.1 High momentum spectrometer

The magnetic spectrometers benefit from relatively small point-to-point uncertainties, which are crucial for absolute cross section measurements. In particular, the optics properties and the acceptance of the HMS have been studied extensively and are well understood in the kinematic e between 0.5 and 5 GeV, as evidenced by more than 200 L/T separations (~ 1000 kinematics) [26]. The position of the elastic peak has been shown to be stable to better than 1 MeV, and the precision rail system and rigid pivot connection have provided reproducible spectrometer pointing for about a decade.

4.2 Photon detection: the neutral particle spectrometer (NPS)

We will use the general-purpose and remotely rotatable NPS system for Hall C. A layout of NPS standing in the SHMS carriage is shown in Fig. 3a. The NPS system consists of the following elements:

- A sweeping magnet providing 0.3 Tm field strength.
- A neutral particle detector consisting of 1080 PbWO_4 crystals in a temperature controlled frame, comprising a 25 msr device at a distance of 4 meters.
- Essentially deadtime-less digitizing electronics to independently sample the entire pulse form for each crystal allowing for background subtraction and identification of pile-up in each signal.
- A new set of high-voltage distribution bases with built-in amplifiers for operation in high-rate environments.
- Cantilevered platforms on the SHMS carriage, to allow for precise and remote rotation around the Hall C pivot of the full photon detection system, over an angle range between 6 and 30 degrees.
- A dedicated beam pipe with as large critical angle as possible to reduce backgrounds beyond the sweeping magnet.

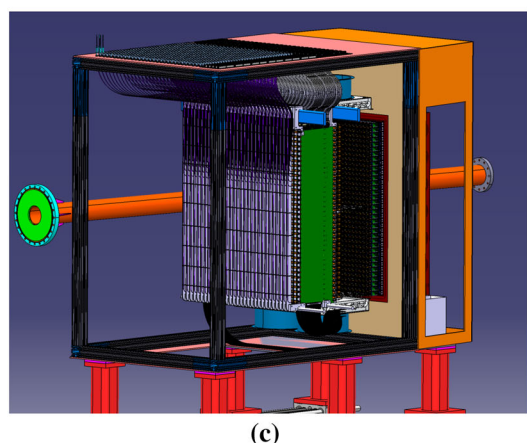
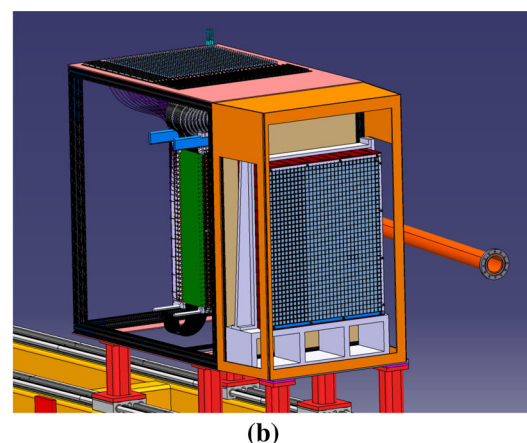
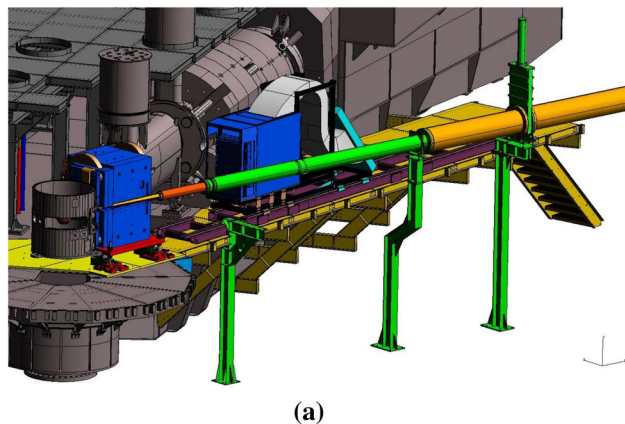


Fig. 3 **a** The DVCS detector in Hall C. The cylinder in the left is the (1 m diameter) vacuum chamber containing the 10-cm long liquid-hydrogen target. The NPS sweeping magnet and calorimeter are standing on the yellow platform of the SHMS, which will be used as carriage to support them. The HMS (not shown) placed on the other side of the beam line will be used to detect the scattered positrons. **b** Front view of the NPS calorimeter showing the PbWO_4 crystal array. **c** Back view of the calorimeter showing the PMT voltage dividers and the vertical PCB distribution boards which bring HV and transfer the PMT signal to the read-out electronics

The PbWO_4 electromagnetic calorimeter

The energy resolution of the photon detection is the limiting factor of the experiment. Exclusivity of the reaction is ensured by the missing mass technique (see Sect. 4.3) and the missing-mass resolution is dominated by the energy resolution of the calorimeter.

We plan to use a PbWO_4 calorimeter 56 cm wide and 68 cm high. This corresponds to 28 by 34 PbWO_4 crystals of 2.05 by 2.05 cm^2 (each 20.0 cm long). We have added one crystal on each side to properly capture showers, and thus designed our PbWO_4 calorimeter to consist of 30 by 36 PbWO_4 crystals, or 60 by 72 cm^2 . This amounts to a requirement of 1080 PbWO_4 crystals.

To reject very low-energy background, a thin absorber could be installed in front of the PbWO_4 detector. The space between the sweeper magnet and the proximity of the PbWO_4 detector will be enclosed within a vacuum channel (with a thin exit window, further reducing low-energy background) to minimize the decay photon conversion in air.

Given the temperature sensitivity of the scintillation light output of the PbWO_4 crystals, the entire calorimeter must be kept at a constant temperature, to within 0.1° to guarantee 0.5% energy stability for absolute calibration and resolution. The high-voltage dividers on the PMTs may dissipate up to several hundred Watts, and this power similarly must not create temperature gradients or instabilities in the calorimeter. The calorimeter will thus be thermally isolated and be surrounded on all four sides by water-cooled copper plates.

At the anticipated background rates, pile-up and the associated baseline shifts can adversely affect the calorimeter resolution, thereby constituting the limiting factor for the beam current. The solution is to read out a sampled signal, and perform offline shape analysis using a flash ADC (fADC) system. New HV distribution bases with built-in pre-amplifiers will allow for operating the PMTs at lower voltage and lower anode currents, and thus protect the photocathodes or dynodes from damage.

The PbWO_4 crystals are $2.05 \times 2.05 \text{ cm}^2$. The typical position resolution is 2–3 mm. Each crystal covers 5 mrad, and the expected angular resolution is 0.5–0.75 mrad, which is comparable with the resolutions of the HMS and SOS, routinely used for Rosenbluth separations in Hall C.

To take full advantage of the high-resolution crystals while operating in a high-background environment, modern flash ADCs will be used to digitize the signal. They continuously sample the signal every 4 ns, storing the information in an internal FPGA memory. When a trigger is received, the samples in a programmable window around the threshold crossing are read out for each crystal that fired. Since the readout of the FPGA does not interfere with the digitizations, the process is essentially deadtime free.

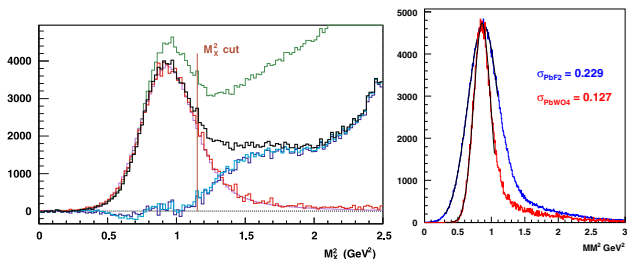


Fig. 4 Left: Missing mass squared in E00-110 for $\text{H}(e, e'\gamma)X$ events (green curve) at $Q^2 = 2.3 \text{ GeV}^2$ and $-t \in [0.12, 0.4] \text{ GeV}^2$, integrated over the azimuthal angle of the photon $\phi_{\gamma\gamma}$. The black curve shows the data once the $\text{H}(e, e'\gamma)\gamma X'$ events have been subtracted. The other curves are described in the text. Right: Projected missing mass resolution for a similar kinematic setting ($E_b = 6.6 \text{ GeV}$, $Q^2 = 3 \text{ GeV}^2$, $x_B = 0.36$). By using PbWO_4 instead of PbF_2 , the missing mass resolution will be considerably improved. Values are given in Table 2 and are to be compared to the the value $\sigma(M_X^2) = 0.2 \text{ GeV}^2$ obtained in previous experiments in Hall A and showed in this figure (left)

Table 1 Estimated systematic uncertainties for the proposed experiment based on previous Hall C experiments

Source	pt-to-pt (%)	scale (%)
Acceptance	0.4	1.0
Electron/positron PID	< 0.1	< 0.1
Efficiency	0.5	1.0
Electron/positron tracking efficiency	0.1	0.5
Charge	0.5	2.0
Target thickness	0.2	0.5
Kinematics	0.4	< 0.1
Exclusivity	1.0	2.0
π^0 subtraction	0.5	1.0
Radiative corrections	1.2	2.0
Total	1.8–1.9	3.8–3.9

4.3 Exclusivity of the DVCS reaction

The exclusivity of the DVCS reaction will be based on the missing mass technique, successfully used during Hall A experiments E00-110 and E07-007 with a PbF_2 calorimeter. Figure 4 presents the missing mass squared obtained in E00-110 for $\text{H}(e, e'\gamma)X$ events, with coincident electron-photon detection.

After subtraction of an accidental coincidence sample, our data is essentially background free: we have negligible contamination of non-electromagnetic events in the HRS and PbF_2 spectra. However, in addition to $\text{H}(e, e'\gamma)p$, we do have the following competing channels: $\text{H}(e, e'\gamma)p\gamma$ from $ep \rightarrow e\pi^0p$, $ep \rightarrow e\pi^0N\pi$, $ep \rightarrow e\gamma N\pi$, $ep \rightarrow e\gamma N\pi\pi \dots$. From symmetric (lab-frame) π^0 -decay, we obtain a high statistics sample of $\text{H}(e, e'\pi^0)X'$ events, with two photon clusters in the PbF_2 calorimeter. From these events, we deter-

Table 2 DVCS kinematics with positrons in Hall C. The incident and scattered beam energies are k and k' , respectively. The calorimeter is centered at the angle θ_{Calo} , which is set equal to the nominal virtual-photon direction. The front face of the calorimeter is at a distance D_{Calo} from the center of the target, and is adjusted to optimize multiple parameters: First to maximize acceptance, second to ensure sufficient separation of the two clusters from symmetric $\pi^0 \rightarrow \gamma\gamma$ decays, and third to ensure that the edge of the calorimeter is never at an angle less than 3.2° from the beam line. The maximum expected positron beam current ($5 \mu\text{A}$) will be used for all kinematics settings. The total amount of beam time needed is 77 days

x_{Bj}	0.2			0.36				0.5			0.6						
$Q^2 (\text{GeV}^2)$	2.0		3.0	3.0			4.0	5.5	3.4	4.8	5.1	6.0					
$E_b (\text{GeV})$	6.6	8.8	11	6.6	8.8	11	8.8	11	8.8	11	6.6	8.8	11				
$k' (\text{GeV})$	1.3	3.5	5.7	3.0	2.2	4.4	6.6	2.9	5.1	2.9	5.2	7.4	5.9				
$\theta_{\text{Calo}} (\text{deg})$	6.3	9.2	10.6	6.3	11.7	14.7	16.2	10.3	12.4	7.9	20.2	21.7	16.6				
$D_{\text{Calo}} (\text{m})$	6	4	6	3			4	3	4		3						
$\sigma_{M_X^2} (\text{GeV}^2)$	0.17		0.22	0.13		0.12	0.15		0.19	0.09		0.11	0.09				
$I_{\text{beam}} (\mu\text{A})$	5																
Days	1	1	3	1	2	3	2	3	4	13	4	3	7	7	2	7	14

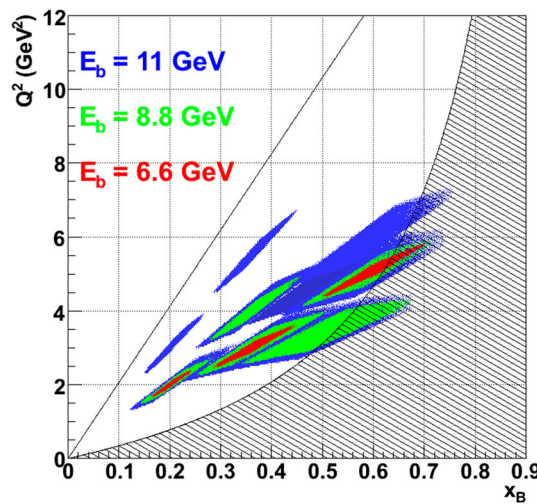


Fig. 5 Display of different kinematic setting proposed. The $Q^2 - x_B$ settings correspond to the ones approved in experiment E12-13-010, which will measure DVCS cross sections using an electron beam. Shaded areas show the resonance region $W < 2 \text{ GeV}$ and the line $Q^2 = (2M_p E_b)x_B$ limits the physical region for a maximum beam energy $E_b = 11 \text{ GeV}$

mine the statistical sample of [asymmetric] $\text{H}(e, e'\gamma)\gamma X$ events that must be present in our $\text{H}(e, e'\gamma)X$ data. The M_X^2 spectrum displayed in black in Fig. 4 was obtained after subtracting this π^0 yield from the total (green) distribution. This is a 14% average subtraction in the exclusive window defined by ' M_X^2 cut' in Fig. 4. Depending on the bin in $\phi_{\gamma\gamma}$ and t , this subtraction varies from 6 to 29%. After our π^0 subtraction, the only remaining channels, of type $\text{H}(e, e'\gamma)N\pi$, $N\pi\pi$, etc. are kinematically constrained to $M_X^2 > (M + m_\pi)^2$. This is the value (' M_X^2 cut' in Fig. 4) we chose for truncating our integration. Resolution effects can cause the inclusive channels to contribute below this cut. To evaluate this possible contamination, during E00-110 we used an additional proton array (PA) of 100 plastic scintillators. The PA subtended a solid angle (relative to the nominal direction of the \mathbf{q} -vector)

of $18^\circ < \theta_{\gamma p} < 38^\circ$ and $45^\circ < \phi_{\gamma p} = 180^\circ - \phi_{\gamma\gamma} < 315^\circ$, arranged in 5 rings of 20 detectors. For $\text{H}(e, e'\gamma)X$ events near the exclusive region, we can predict which block in the PA should have a signal from a proton from an exclusive $\text{H}(e, e'\gamma p)$ event. The red histogram is the $X = (p + y)$ missing mass squared distribution for $\text{H}(e, e'\gamma p)_y$ events in the predicted PA block, with a signal above an effective threshold 30 MeV (electron equivalent). The blue curve shows our inclusive yield, obtained by subtracting the normalized triple coincidence yield from the $\text{H}(e, e'\gamma)X$ yield. The (smooth) violet curve shows our simulated $\text{H}(e, e'\gamma)p$ spectrum, including radiative and resolution effects, normalized to fit the data for $M_X^2 \leq M^2$. The cyan curve is the estimated inclusive yield obtained by subtracting the simulation from the data. The blue and cyan curves are in good agreement, and show that our exclusive yield has less than 2% contamination from inclusive processes.

In this proposed experiment we plan to use a PbWO_4 calorimeter with a resolution more than twice better than the PbF_2 calorimeter used in E00-110. While the missing mass resolution will be slightly worse at some high beam energy, low x_B kinematics, the better energy resolution of the crystals will largely compensate for it, and the missing mass resolution in this experiment will be significantly better than ever before. Figure 4 (right) shows the missing mass resolution for PbF_2 and PbWO_4 for a kinematic setting similar to the one measured in Hall A. Table 2 shows the missing mass resolution projected for each of the settings using the proposed PbWO_4 calorimeter.

4.4 Systematics uncertainties

The HMS is a very well understood magnetic spectrometer which will be used here with modest requirements (beyond the momentum), defining the (x_B, Q^2) kinematics well. Table 1 shows the estimated systematic uncertainties

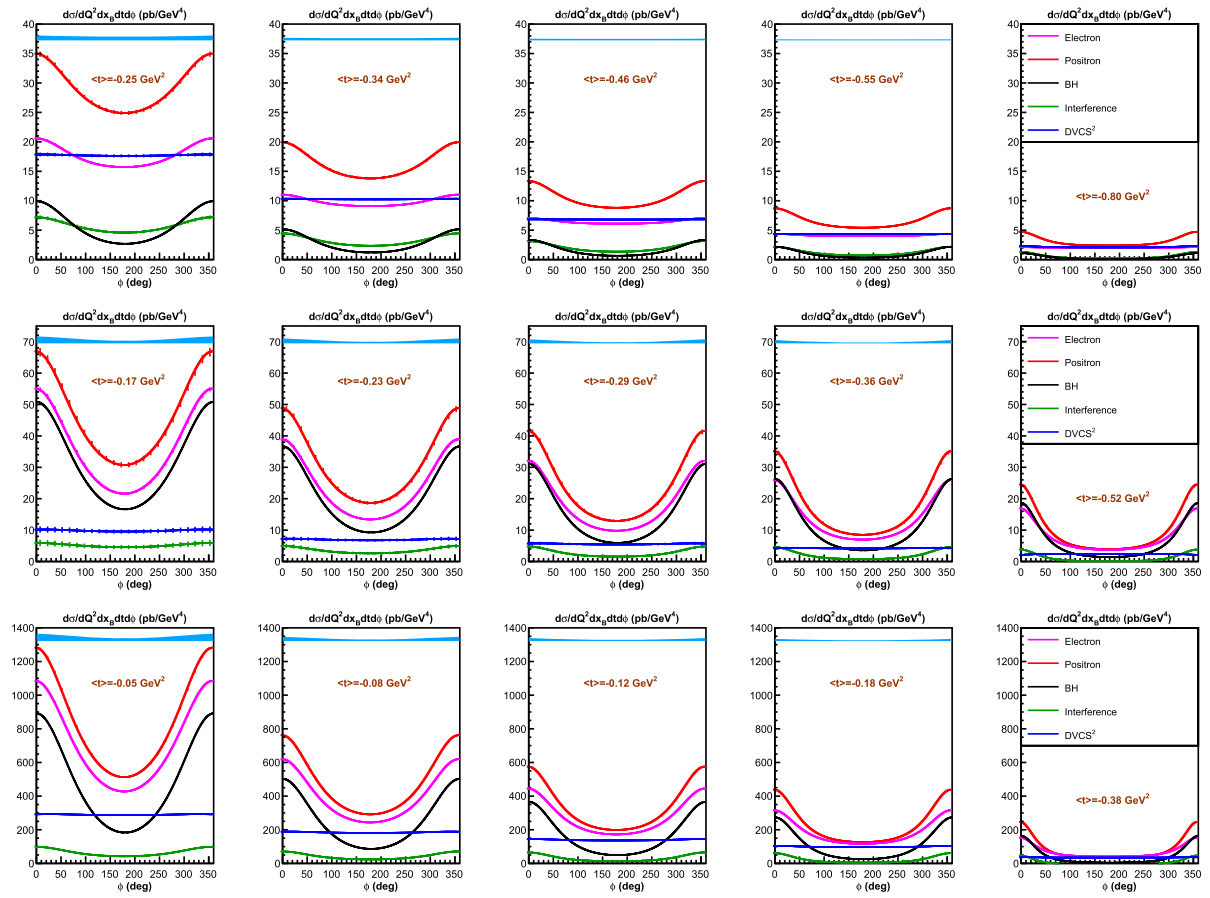


Fig. 6 Experimental projections for 3 different of the settings proposed: $x_B = 0.2$, $Q^2 = 2.0 \text{ GeV}^2$ (top), $x_B = 0.36$, $Q^2 = 4.0 \text{ GeV}^2$ (middle) and $x_B = 0.5$, $Q^2 = 3.4 \text{ GeV}^2$ (bottom). Red points show the projected positron cross sections with statistical uncertainties. Electron cross sections that will be measured in experiment E12-13-010 are

shown in magenta. The combination of e^- and e^+ cross sections allow the separation of the DVCS² contribution (blue) and the DVCS-BH interference (green). For reference, the BH cross section is displayed in black. Systematic uncertainties are shown by the cyan band

for the proposed experiment based on previous experience from Hall C equipment and Hall A experiments.

5 Proposed kinematics and projections

Table 2 details the kinematics and beam time used in the projection. Q^2 scans at 4 different values of x_B were chosen in kinematics with already approved electron data [18]. The positron beam current assumed is $5 \mu\text{A}$ (unpolarized beam) and is currently the limiting factor driving the beam time needs.

Considering a 1 mA initial electron beam, $5 \mu\text{A}$ of positrons corresponds to the maximum positron to electron ratio produced by 123 MeV electrons [27]. This also corresponds to the lowest polarization transfer to the positrons, which will be considered unpolarized in our projections.

Beam time in Table 2 is calculated in order collect positron data corresponding to $\sim 25\%$ of the approved electron data.

The different kinematics settings are represented in Fig. 5 in the Q^2-x_B plane. The area below the straight line $Q^2 = (2M_p E_b)x_B$ corresponds to the physical region for a maximum beam energy $E_b = 11 \text{ GeV}$. Also plotted is the resonance region $W < 2 \text{ GeV}$.

We have performed detailed Monte Carlo simulation of the experimental setup and evaluated counting rates for each of the settings. In order to do this, we have used a recent global fit of world data with LO sea evolution by Müller and Kumerički [28]. This fit reproduces the magnitude of the DVCS cross section measured in Hall A at $x_B = 0.36$ and is available up to values of $x_B \leq 0.5$. For our high x_B settings we used a GPD parametrization by Kroll et al. [29] fitted to Deeply Virtual Meson Production data, together with a code to compute DVCS cross sections, provided by Moutarde [30]. Notice that for DVCS, counting rates and statistical uncertainties will be driven *at first order* by the Bethe–Heitler (BH) cross section, which is well-known.

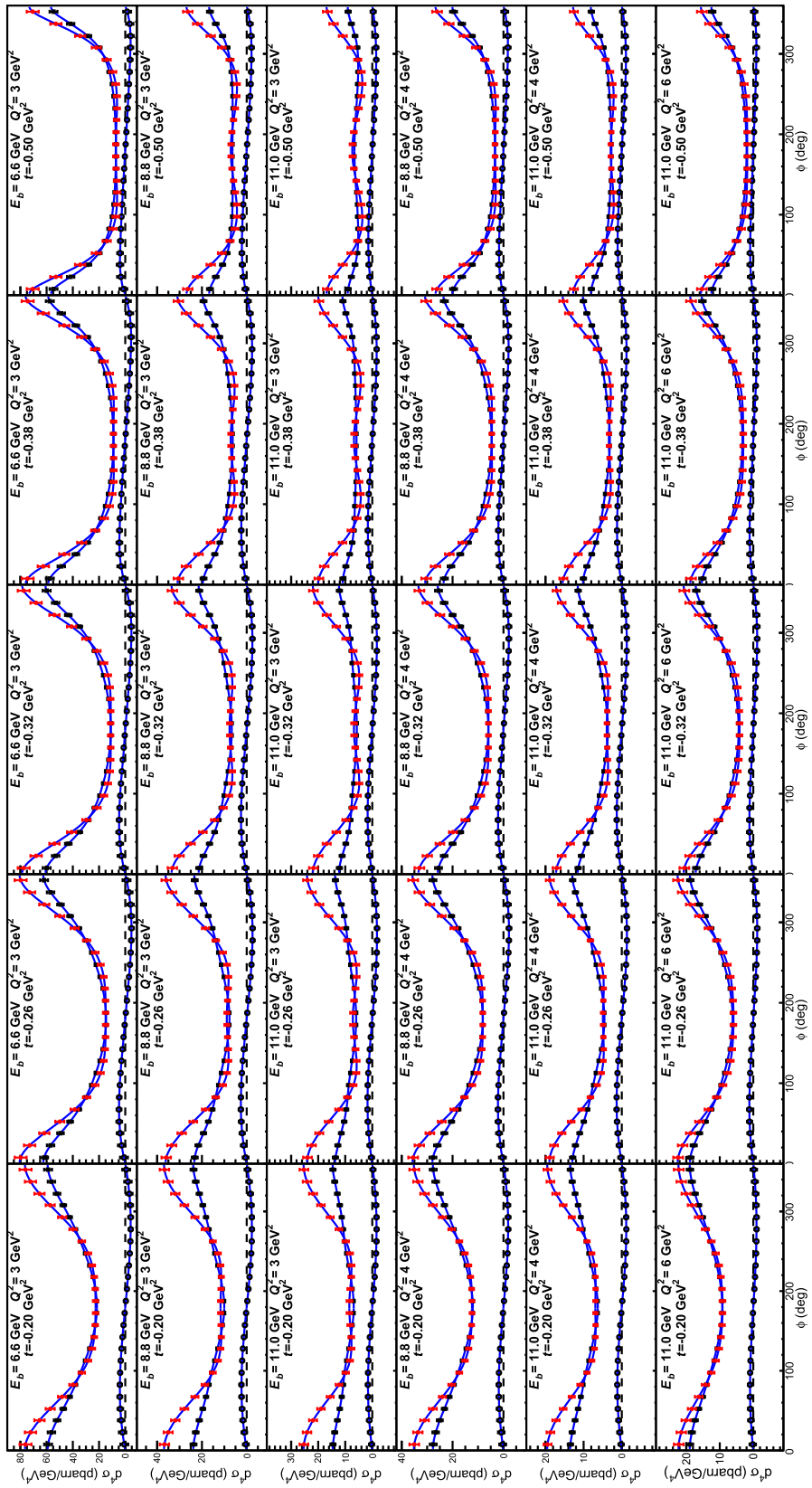


Fig. 7 Fits of data with $x_B = 0.36$. Each row shows five kinematic settings in Q^2 at constant x_B and t . Each column corresponds to 5 different bins in t . The blue lines are simultaneous fits of the (approved) electron data, both the helicity-dependent (black squares) and helicity-independent (black circles) cross sections, and the (proposed) positron data (red points). Horizontal dashed lines in each panel indicate the origin of the vertical axis: $d^4\sigma = 0$

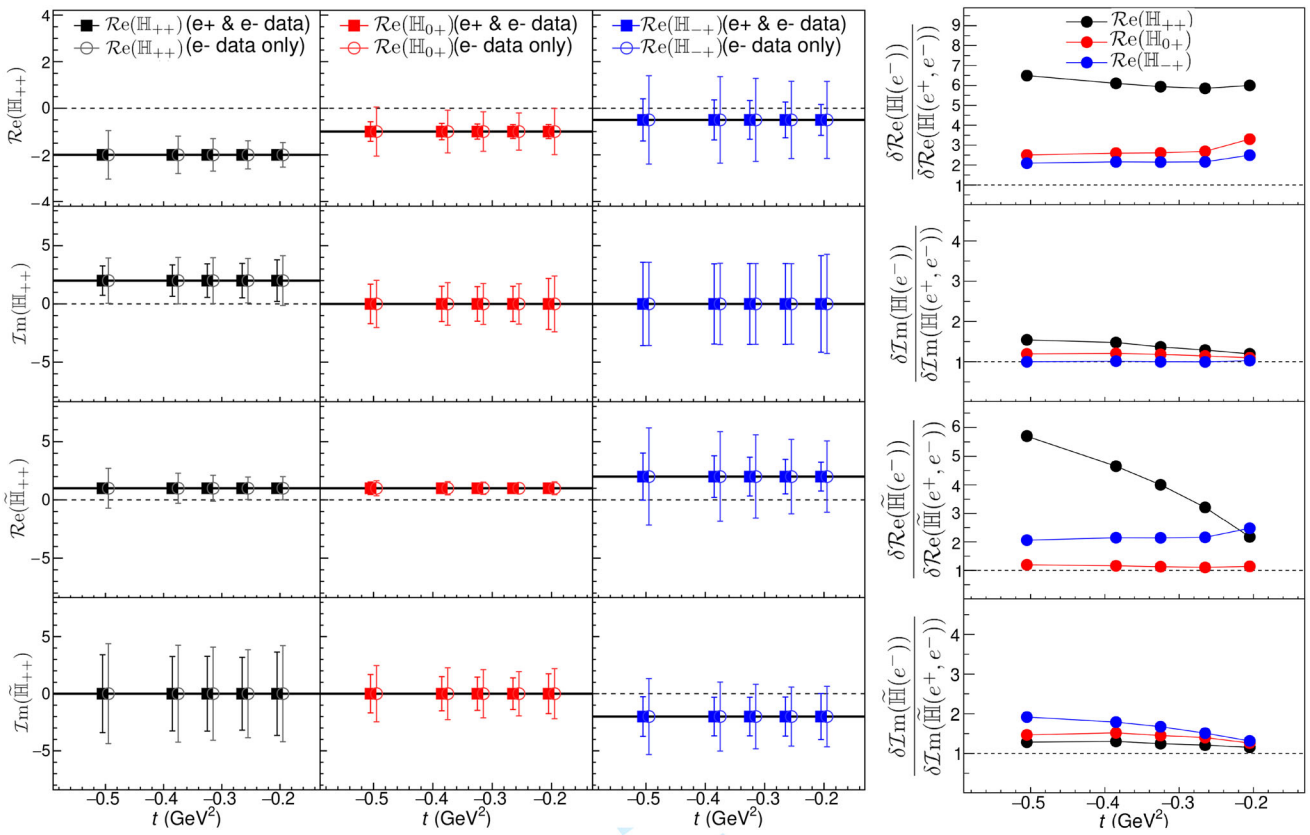


Fig. 8 CFFs extracted from the fits in Fig. 7. Left: the first column in the left shows the results of the helicity-conserving CFFs when both positron and electron data are used in the fit (black), and when only the electron approved data is used (grey). The second and third columns

show the same information for the helicity-flip CFFs. The solid horizontal lines indicate the input values used to generate the cross-section data. Right: ratio of the uncertainties between the fit using both electron and positron data and the one using only electron data

Figure 6 shows the projected results for 3 selected settings at different values of $x_B = 0.2, 0.36, 0.5$. Statistical uncertainties are shown by error bars and systematic uncertainties are represented by the cyan bands.

The DVCS² term (which is ϕ independent at leading twist) can be very cleanly separated from the BH-DVCS interference contribution, and this without any assumption regarding the leading-twist dominance. The Q^2 -dependence of each term will be measured (cf. Table 2) and its dependence compared to the asymptotic prediction of QCD. The extremely high statistical and systematic precision of the results illustrated in Fig. 6 will be crucial to disentangle higher order effects (higher twist or next-to-leading order contributions) as shown by recent results [17].

6 Constraints on Compton form factors

In order to quantify the impact of the proposed experiment on the extraction of the nucleon Compton Form Factors, we have simulated the extraction of the proton CFFs by using

only approved electron cross-section measurements (both helicity-dependent and helicity-independent) from upcoming experiment E12-13-010 and with the addition of the positron measurements proposed herein. Measurements with an unpolarized target as proposed herein have little sensitivity to GPDs E and \tilde{E} . Therefore, only the CFFs corresponding to H and \tilde{H} have been fitted. Prospects of measurements with polarized targets would be, of course, extremely exciting and complementary to these. Most importantly, as mentioned before, kinematics corrections of $\mathcal{O}(t/Q^2)$ and $\mathcal{O}(M^2/Q^2)$ cannot be neglected in JLab kinematics. Therefore, all CFFs H_{++} , H_{0+} , H_{-+} , \tilde{H}_{++} , \tilde{H}_{0+} and \tilde{H}_{-+} have been fitted.

First of all, the DVCS cross sections measured in Hall A with a 6 GeV beam [17, 31] were fitted in order to extract some realistic values of the CFFs. These values were then used to calculate projected cross sections at the kinematics of Table 2. The CFFs are assumed constant in t for this exercise and equal to the average value of those extracted from 6 GeV data. The projected electron and positron cross sections are then fitted. In doing this, the statistical and systematic uncertainties of the measurements were added quadratically.

Figure 7 shows the results for kinematics with $x_B = 0.36$. Each line shows the five kinematic settings in Q^2 , E_b at constant x_B and t , which are fitted simultaneously neglecting the logarithmic Q^2 -dependence of CFFs in the range of $\sim 3\text{--}6$ GeV 2 . In addition to the five independent terms on the azimuthal angle (~ 1 , $\sim \cos \phi$, $\sim \cos 2\phi$, $\sim \sin \phi$ and $\sim \sin 2\phi$), three different beam energies are fitted simultaneously.

Each column in Fig. 7 shows each of the 5 bins in t where the data were binned. The blue lines correspond to the fits of both the (approved) electron data (helicity-dependent and helicity-independent) and the positron (proposed) data (only helicity-independent). Notice that the NPS calorimeter acceptance will allow a full coverage in ϕ for the bins in t presented.

Results of the CFFs extracted from the fits are shown in Fig. 8. The first column in the left shows the results of the helicity-conserving CFFs when both positron and electron data are used in the fit, and when only the electron approved data are used. The second and third columns show the same information for the helicity-flip CFFs. The solid horizontal lines in each panel indicate the input values used to generate the cross-section data, which are then accurately extracted by the fit. The ratio of the uncertainties between the fit using both electron and positron data and the one using only electron data is shown in the last column on the right. One can see the significant improvement of positron data: a factor of 6 for $\mathcal{R}](\mathbb{H}_{++})$ and an average factor of 4 for $\mathcal{R}](\tilde{\mathbb{H}}_{++})$. There is also a factor ~ 2 improvement in the real part of most helicity-flip CFFs. The imaginary part of CFFs are not impacted by these positron data – this is expected as no helicity-dependent positron cross sections are used in the fits.

In addition to reducing the uncertainties of the fitted CFFs, positron data also improves the correlation of the extracted parameters. Figure 9 shows the correlation coefficient between the different pairs of CFFs as extracted from the electron data alone (left) and with the addition of positron data (right). The correlation coefficient for each pair of extracted CFFs ($\mathbb{F}_i, \mathbb{F}_j$) is defined as $\rho_{i,j} = \text{cov}[\mathbb{F}_i, \mathbb{F}_j]/(\sigma_i \sigma_j)$. It varies from -1 to 1 . and Fig. 9 reports its absolute value. One can notice, in particular, that while the helicity-conserving real parts of $\mathbb{H}_{+,+}$ and $\tilde{\mathbb{H}}_{+,+}$ are very correlated in the case of a fit with electron data only, the correlation is significantly reduced when positron data are included. The improvement varies from -98 to -54% at the highest value of $|t|$ and from -70 to -24% at the lowest $|t|$.

7 Summary

We propose to measure the cross section of the DVCS reaction accurately using positrons in the wide range of kinematics allowed by a set of beam energies up to 11 GeV. We will

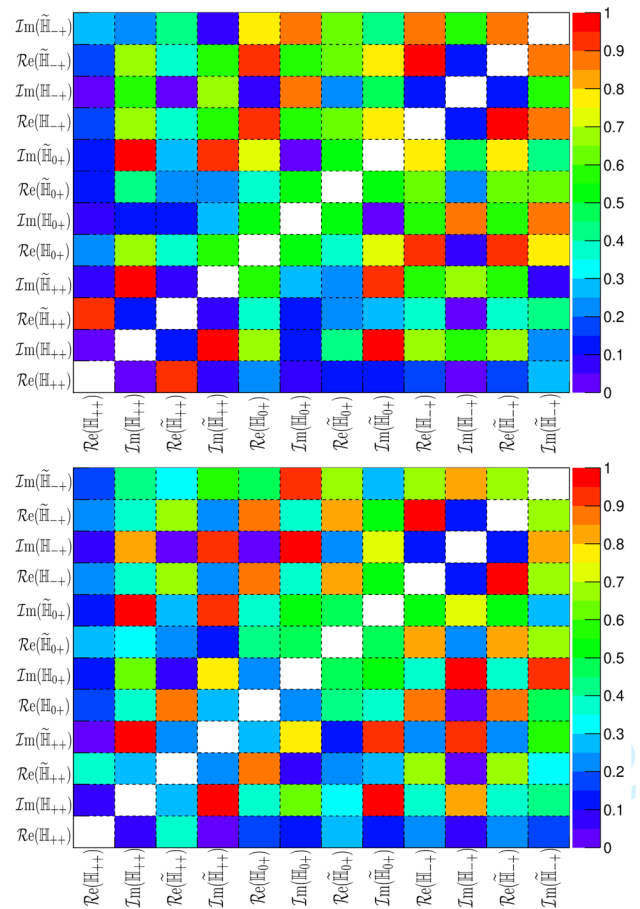


Fig. 9 Magnitude of the correlation coefficients between the different CFFs extracted from the fit of DVCS electron data (top) and from the combined fit of DVCS electron and positron data (bottom). Plots correspond to bin $x_B = 0.36$ and $t = -0.26$ GeV 2 . The correlation between $\mathcal{R}](\mathbb{H}_{+,+})$ and $\mathcal{R}](\tilde{\mathbb{H}}_{+,+})$ goes from -94% without positrons to -39% when electron and positrons are combined

exploit the beam charge dependence of the cross section to separate the contribution of the BH-DVCS interference and the DVCS 2 terms.

The Q^2 -dependence of each individual term will be measured and compared to the predictions of the handbag mechanism. This will provide a quantitative estimate of higher-twist effects to the GPD formalism in JLab kinematics.

The combination of measurements with electrons and positrons allow to much better constrain the Compton Form Factors measurements and reduce significantly the correlations in the extracted values.

We plan to use Hall C High-Momentum Spectrometer, combined with a high resolution PbWO₄ electromagnetic calorimeter.

In order to complete this full mapping of the DVCS cross section with positrons over a wide range of kinematics, we require 77 days of (unpolarized) positron beam ($I > 5\mu\text{A}$).

Acknowledgements This material is based upon work supported by the U.S. Department of Energy, Office of Science, Office of Nuclear Physics under contract DE-AC05-06OR23177.

Data Availability Statement This manuscript has no associated data or the data will not be deposited. [Authors' comment: Data sharing not applicable to this article as no datasets were generated or analysed during the current study.]

References

1. J.C. Collins, A. Freund, Proof of factorization for deeply virtual compton scattering in QCD. *Phys. Rev. D* **59**, 074009 (1999)
2. X.-D. Ji, J. Osborne, One-loop corrections and all order factorization in deeply virtual Compton scattering. *Phys. Rev. D* **58**, 094018 (1998)
3. D. Mueller, D. Robaschik, B. Geyer, F.M. Dittes, J. Horejsi, Wave functions, evolution equations and evolution kernels from light-ray operators of QCD. *Fortschr. Phys.* **42**, 101 (1994)
4. X.-D. Ji, Deeply virtual Compton scattering. *Phys. Rev. D* **55**, 7114–7125 (1997)
5. X.-D. Ji, Gauge invariant decomposition of nucleon spin. *Phys. Rev. Lett.* **78**, 610–613 (1997)
6. J. Xiang-Dong, W. Melnitchouk, X. Song, A Study of off forward parton distributions. *Phys. Rev. D* **56**, 5511–5523 (1997)
7. A.V. Radyushkin, Nonforward parton distributions. *Phys. Rev. D* **56**, 5524–5557 (1997)
8. A.V. Radyushkin, Scaling limit of deeply virtual Compton scattering. *Phys. Lett. B* **380**, 417–425 (1996)
9. A.V. Belitsky, D. Mueller, A. Kirchner, Theory of deeply virtual Compton scattering on the nucleon. *Nucl. Phys.* **B629**, 323–392 (2002)
10. M. Diehl, *Eur. Phys. J. C* **25**, 223–232 (2002)
11. O.V. Teryaev, Analytic properties of hard exclusive amplitudes, in 11th International Conference on Elastic and Diffractive Scattering. eprint. [arXiv: hep-ph/0510031](https://arxiv.org/abs/hep-ph/0510031) (2005)
12. I.V. Anikin, O.V. Teryaev, Dispersion relations and subtractions in hard exclusive processes. *Phys. Rev. D* **76**, 056007 (2007)
13. I.V. Anikin, O.V. Teryaev, Dispersion relations and QCD factorization in hard reactions. *Fizika B* **17**, 151–158 (2008)
14. M. Diehl, D.Yu. Ivanov, *Eur. Phys. J. C* **52**, 919–932 (2007)
15. M.V. Polyakov, C. Weiss, Skewed and double distributions in pion and nucleon. *Phys. Rev. D* **60**, 114017 (1999)
16. M. Diehl, T. Gousset, B. Pire, J.P. Ralston, Testing the handbag contribution to exclusive virtual Compton scattering. *Phys. Lett. B* **411**, 193–202 (1997)
17. M. Defurne et al., A glimpse of gluons through deeply virtual Compton scattering on the proton. *Nat. Commun.* **8**(1), 1408 (2017)
18. C. Muñoz Camacho, T. Horn, C. Hyde, R. Paremuzyan, J. Roche et al., Jefferson Lab experiment proposal E12–13–010. https://hallaweb.jlab.org/experiment/DVCS/documents/proposals/E12-13-010_proposal.pdf
19. A.V. Belitsky, D. Mueller, Exclusive electroproduction revisited: treating kinematical effects. *Phys. Rev. D* **82**, 074010 (2010)
20. A. Airapetian et al., The Beam-charge azimuthal asymmetry and deeply virtual Compton scattering. *Phys. Rev. D* **75**, 011103 (2007)
21. V.M. Braun, A.N. Manashov, D. Mueller, B.M. Pire, Deeply virtual Compton scattering to the twist-four accuracy: impact of finite-*t* and target mass corrections. *Phys. Rev. D* **89**(7), 074022 (2014)
22. K. Kumericki, D. Mueller, Deeply virtual Compton scattering at small x(B) and the access to the GPD H. *Nucl. Phys. B* **841**, 1–58 (2010)
23. K. Kumericki, S. Liuti, H. Moutarde, GPD phenomenology and DVCS fitting. *Eur. Phys. J. A* **52**(6), 157 (2016)
24. R. Dupre, M. Guidal, M. Vanderhaeghen, Tomographic image of the proton. *Phys. Rev. D* **95**(1), 011501 (2017)
25. A.V. Belitsky, D. Mueller, Y. Ji, Compton scattering: from deeply virtual to quasi-real. *Nucl. Phys. B* **878**, 214–268 (2014)
26. Y. Liang et al., in Proceedings of the 9th International Conference on the Structure of Baryons (2002)
27. L.S. Cardman, The PEPPo method for polarized positrons and PEPPo II. *AIP Conf. Proc.* **1970**(1), 050001 (2018)
28. DD. Müller, K. Kumericki, Model 3. <http://calculon.phy.pmf.unizg.hr/gpd/>
29. P. Kroll, H. Moutarde, F. Sabatie, From hard exclusive meson electroproduction to deeply virtual Compton scattering. *Eur. Phys. J. C* **73**, 2278 (2013)
30. B. Berthou et al., PARTONS: PARtonic tomography of nucleon software: a computing platform for the phenomenology of generalized parton distributions. *Eur. Phys. J. C* **78**, 478 (2018)
31. M. Defurne et al., E00–110 experiment at Jefferson Lab Hall A: deeply virtual Compton scattering off the proton at 6 GeV. *Phys. Rev. C* **92**(5), 055202 (2015)